

Spin Dynamics in Hierarchical Black Hole Triples: Predicting Final Spin-Orbit Misalignment Angle From Initial Conditions

YUBO SU,¹ DONG LAI,¹ AND BIN LIU¹

¹*Cornell Center for Astrophysics and Planetary Science, Department of Astronomy, Cornell University, Ithaca, NY 14853, USA*

(Received XXXX; Revised XXXX; Accepted XXXX)

Submitted to ApJL

ABSTRACT

Abstract

Keywords: keywords

1. INTRODUCTION—WORK IN PROGRESS DO NOT READ

Para 1: (see papers Liu-Lai, can copy/adapt) The standard scenario for the formation merging BH binaries involve isolated binary evolution, in which mass transfer and friction in the common envelope phase bring the binar closer (TODO) The recent detections of (TODO) by LIGO have motivated the studies of various alternative, dynamical formation channels (TODO) One of the dynamical channels is "tertiary-induced mergers", in which (TODO)

Para 2: One of the ways to distinguish different channels is spin (TODO). Introduce χ_{eff} (TODO)

Para 3: In a recent paper, Liu et al found that LK-induced mergers can often lead to a "90° spin attractor": Starting for aligned spi-orbit, the inner binary eventually evolves toward (TODO) This "attractor" requires the LK-induced orbital evolution/decay to be slow and regular, and octupole effect not important. Figure 1 (your current 3) gives an exmaple (TODO) Figure 2 (your current Fig.2) shows (TODO).

Para 4: The physical origin of this "90 spin attractor" is not understood. Liu et al proposed an explanation based on analogy with an adiabatic invariant in circular systems where the tertiary make the inner binary process but does not induce eccentricity oscillation (Liu-Lai 2017). But this adiabatic invariant cannot be applied to LK-induced mergers, where e-excitation lays a crucial role (TODO) In addition, Liu-Lai (2017) considered found that for "mild LK-enhanced mergers", the attractor does not exist (TODO).despite the fcst that the orbital evolution is slow and regular (TODO)

Para 5: In this paper we examine the theory that explain the attractor, as well as the regime of validity (TODO).

In Section 2, we set up the relevant equations of motion for the orbital and spin evolution of the three BHs, and we argue for the primary result of the paper, conservation of the angle θ_e . In Sections 4 and 5, we consider two scenarios under which conservation of θ_e can be violated. We discuss and conclude in Section 6.

2. LK-INDUCED MERGERS: ORBITAL EVOLUTION

We study Lidov-Kozai (LK) oscillations due to an external perturber to quadrupole order and include apsidal precession and gravitational wave radiation due to general relativity. Consider an black hole (BH) binary with masses m_1 and m_2 having total mass m_{12} and reduced mass μ orbiting a super-massive black hole (SMBH) with mass $m_3 \gg m_1$ and m_2 . Call a_3 and e_3 the semimajor axis and eccentricity of the orbit of the inner binary around the SMBH, and define effective semimajor axis

$$\tilde{a}_3 \equiv a_3 \sqrt{1 - e_3^2}. \quad (1)$$

Finally, call $\mathbf{L}_{\text{out}} \equiv L_{\text{out}} \hat{\mathbf{L}}_{\text{out}}$ the angular momentum of the SMBH relative to the center of mass of the inner BH binary, and call $\mathbf{L} \equiv L \hat{\mathbf{L}}$ the orbital angular momentum of the inner BH binary. We take \mathbf{L}_{out} to be fixed.

We then consider the motion of the inner binary, described by the Keplerian orbital elements $(a, e, \varpi, I, \omega)$ (respectively: semimajor axis, eccentricity, longitude of the ascending node, inclination, and argument of periapsis). The equations describing the motion of these orbital elements are (Peters 1964;

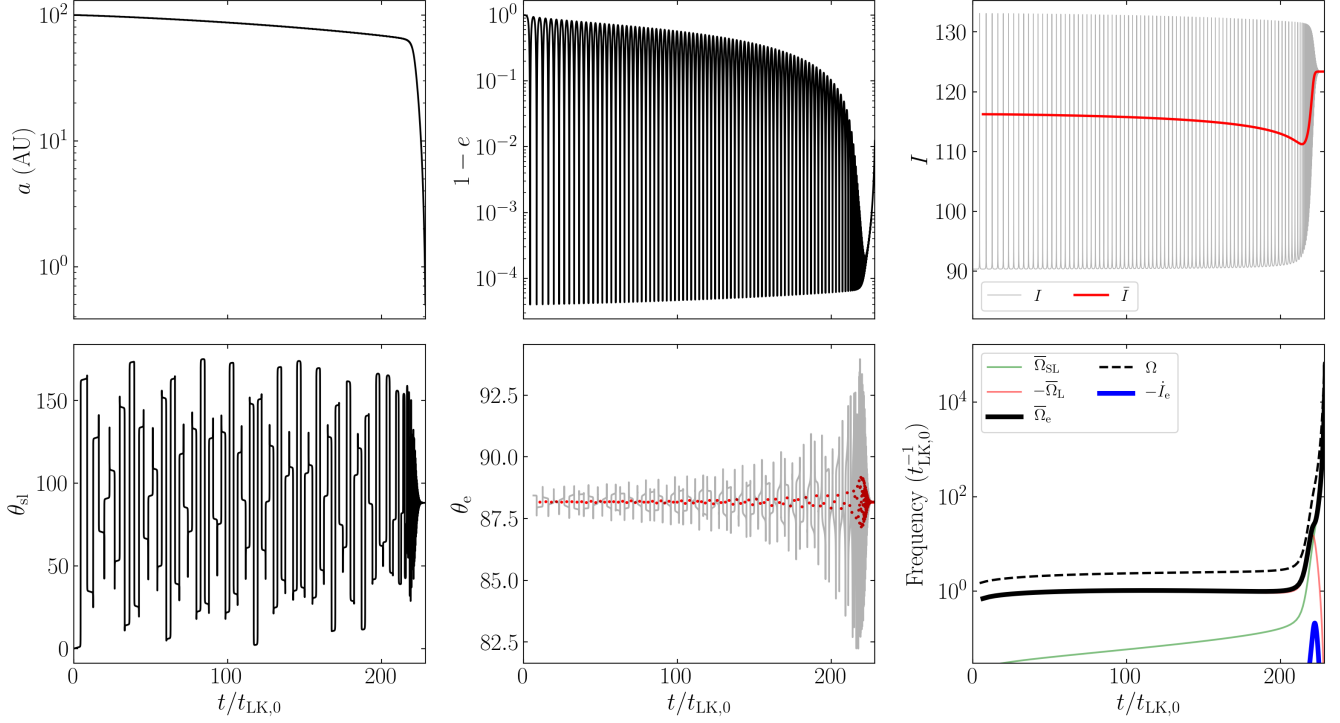


Figure 1. Orbital and spin evolution in a system for which the total change in the adiabatic invariant θ_e is $\lesssim 0.01^\circ$. The unit of time $t_{\text{LK},0}$ is the LK timescale [Eq. (7)] evaluated for the initial conditions. The inner binary is taken to have $a = 100$ AU, $m_1 = 30M_\odot$, $m_2 = 20M_\odot$, $I_0 = 90.35^\circ$, and $e_0 = 0.001$, while the tertiary SMBH has $\tilde{a}_3 = 2.2$ pc, $m_3 = 3 \times 10^7 M_\odot$. We take $\theta_{\text{sl}}^i = 0$. The top three panels a ; e ; and the inclination of the inner binary, both instantaneous (I) and appropriately averaged following Eq. (27) (\bar{I}). The bottom three panels show the instantaneous spin-orbit misalignment angle θ_{sl} ; the angle between $\hat{\Omega}_e$ [Eq. (23)] and both the instantaneous spin vector (light grey) and the LK-averaged spin vector [red dots, denoted θ_e , Eq. (34)]; and four characteristic frequencies of the system [Eqs. 23 and (24)].

Storch & Lai 2015; Liu & Lai 2018)

where we define

$$t_{\text{LK}}^{-1} = n \left(\frac{m_3}{m_{12}} \right) \left(\frac{a}{\tilde{a}_3} \right)^3, \quad (7)$$

$$\left(\frac{da}{dt} \right)_{\text{GW}} = -\frac{a}{t_{\text{GW}}(e)}, \quad (8)$$

$$t_{\text{GW}}^{-1}(e) = \frac{64}{5} \frac{G^3 \mu m_{12}^2}{c^5 a^4} \frac{1}{(1-e^2)^{7/2}} \left(1 + \frac{73}{24} e^2 + \frac{37}{96} e^4 \right), \quad (9)$$

$$\left(\frac{de}{dt} \right)_{\text{GW}} = -\frac{304}{15} \frac{G^3 \mu m_{12}^2}{c^5 a^4} \frac{1}{(1-e^2)^{5/2}} \left(1 + \frac{121}{304} e^2 \right), \quad (10)$$

$$\Omega_{\text{GR}} = \frac{3Gnm_{12}}{c^2 a (1-e^2)}, \quad (11)$$

and $n = \sqrt{Gm_{12}/a^3}$ is the mean motion of the inner binary. We will often refer to e_{min} and e_{max} the minimum/maximum eccentricity in a single LK cycle, and we will sometimes notate $j(e) = \sqrt{1-e^2}$ and $j(e_{\text{max}}) = \sqrt{1-e_{\text{max}}^2}$.

Finally, for concreteness, we adopt fiducial parameters similar to those from Liu & Lai (2018): the inner binary has $a = 100$ AU, $m_1 = 30M_\odot$, $m_2 = 20M_\odot$, and initial $e_0 = 0.001$ with varying I_0 . We take the SMBH tertiary companion to

$$\frac{da}{dt} = \left(\frac{da}{dt} \right)_{\text{GW}}, \quad (2)$$

$$\frac{de}{dt} = \frac{15}{8t_{\text{LK}}} e \sqrt{1-e^2} \sin 2\omega \sin^2 I + \left(\frac{de}{dt} \right)_{\text{GW}}, \quad (3)$$

$$\frac{d\Omega}{dt} = \frac{3}{4t_{\text{LK}}} \frac{\cos I (5e^2 \cos^2 \omega - 4e^2 - 1)}{\sqrt{1-e^2}}, \quad (4)$$

$$\frac{dI}{dt} = \frac{15}{16} \frac{e^2 \sin 2\omega \sin 2I}{\sqrt{1-e^2}}, \quad (5)$$

$$\frac{d\omega}{dt} = \frac{3}{4t_{\text{LK}}} \frac{2(1-e^2) + 5 \sin^2 \omega (e^2 - \sin^2 I)}{\sqrt{1-e^2}} + \Omega_{\text{GR}}, \quad (6)$$

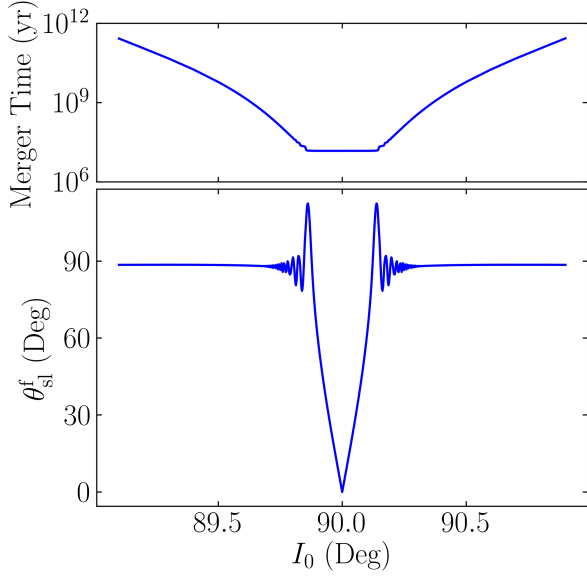


Figure 2. Plot of merger time of the inner binary and θ_{sl}^f for $m_1 = 30M_\odot$, $m_2 = 20M_\odot$, $m_3 = 3 \times 10^7 M_\odot$, $a_{\text{in}} = 100$ AU, $\tilde{a}_3 = 2.2$ pc, $e_3 = 0$, where $e_0 = 0.001$ and $\theta_{\text{sl}}^i = 0$ over a restricted range of I_0 (analogous to the bottom-most panel in Fig. 3 of Liu & Lai 2018), where the blue dots are taken from numerical simulations. It is clear that for I_0 sufficiently far from 90° , the resulting θ_{sl}^f are quite similar and are near 90° (Liu & Lai 2018).

have $m_3 = 3 \times 10^7 M_\odot$ and $\tilde{a}_3 = 4.5 \times 10^5$ AU = 2.2 pc. This gives the same t_{LK} as in Liu & Lai (2018).

We summarize a few key analytical properties of this orbital evolution below:

- Neglecting GR effects (GW radiation and apsidal precession), the above equations describe periodic oscillations in e and I . There are two conserved quantities, the total angular momentum $\mathbf{L}_{\text{out}} + \mathbf{L}$ and the “Kozai constant” (Lidov 1962; Kozai 1962):

$$K \equiv j(e) \cos I. \quad (12)$$

This implies that e is a function of ω only.

Note that an eccentricity maximum occurs every half-period of ω , at $\omega = \pi/2$ and $\omega = 3\pi/2$ (Anderson et al. 2016). It is most convenient to define the LK period P_{LK} as the half-period of ω . Then we define characteristic LK frequency

$$\Omega \equiv \frac{2\pi}{P_{\text{LK}}}. \quad (13)$$

The conservation laws above can be combined to calculate the maximum eccentricity as a function of I . If the minimum eccentricity is negligible, then

$$e_{\text{max}} \equiv \sqrt{1 - \frac{5}{3} \cos^2 I_0}. \quad (14)$$

Note that these results assume $L_{\text{out}} \gg L$ and that both octupole and GR effects are negligible; see Liu & Lai (2018) for generalized forms of the above results.

Finally, when $e_{\text{min}} \ll e_{\text{max}}$, the binary spends a fraction $\sim j(e_{\text{max}})$ of the LK cycle near $e \simeq e_{\text{max}}$ (Anderson et al. 2016).

- When GR effects are considered, the system gradually coalesces due to GW radiation, primarily near eccentricity maxima. This process is governed by three competing timescales: (i) LK oscillations ($\sim j(e_{\text{max}})t_{\text{LK}}$), (ii) apsidal precession due to post-Newtonian effects ($\sim \Omega_{\text{GR}}^{-1}(e_{\text{max}})$), and (iii) orbital decay due to GW radiation ($\sim t_{\text{GW}}(e_{\text{max}})$). At early times, (i) is the shortest, but as a decreases, (ii) and (iii) become dominant and eccentricity oscillations become suppressed, which we term “eccentricity freezing”. We consider the two conditions under which this happens.

Apsidal precession becomes important when Ω_{GR} is the dominant contribution in Eq. (6). Quantitatively, this occurs when

$$\frac{\epsilon_{\text{GR}}}{j(e_{\text{max}})} \gg 1, \quad (15)$$

where we define

$$\epsilon_{\text{GR}} \equiv \frac{3Gm_{12}^2 \tilde{a}_3^3}{c^2 m_3 a^4}. \quad (16)$$

GW radiation can also inhibit eccentricity oscillations when $t_{\text{LK}}j(e) \gtrsim t_{\text{GW}}(e)$ [see Eq. (3)]. In order for GW radiation to be the dominant source of eccentricity freezing, we require

$$1 \lesssim \frac{t_{\text{GW}}^{-1}(e)}{\Omega_{\text{GR}}} \sim \left(\frac{Gm_{12}}{a(1-e^2)c^2} \right)^{3/2} \frac{1}{1-e^2}, \quad (17)$$

$$\sim \left(\frac{v_p}{c} \right)^3 \frac{1}{1-e^2}, \quad (18)$$

where v_p is the pericenter velocity of the inner binary. Since $v_p/c \ll 1$, we find that apsidal precession is usually more effective at freezing the eccentricity.

The behavior of a , e , and I for a characteristic LK-induced merger can be seen in Fig. 1. At early times, e and I have large oscillations while a slowly decreases. At later times, e and I stop oscillating as apsidal precession freezes the eccentricity, and both a and e decrease under GW radiation. Since P_{LK} is defined as the half-period in ω , it asymptotes to Ω_{GR} at late times even though the eccentricity is frozen (bottom right panel of Fig. 1).

3. SPIN DYNAMICS: EQUATIONS

We are ultimately interested in the spin orientations of the inner BHs at merger as a function of initial conditions. Since they evolve independently to leading post-Newtonian order, we focus on the dynamics of a single BH spin $\hat{\mathbf{S}}$. Since the spin magnitude does not enter into the dynamics, we write $\mathbf{S} \equiv \hat{\mathbf{S}}$ for brevity (i.e. \mathbf{S} is a unit vector). Neglecting spin-spin interactions, \mathbf{S} undergoes de Sitter precession about \mathbf{L} as

$$\frac{d\mathbf{S}}{dt} = \Omega_{\text{SL}} \hat{\mathbf{L}} \times \mathbf{S}, \quad (19)$$

$$\Omega_{\text{SL}} = \frac{3Gn(m_2 + \mu/3)}{2c^2 a (1 - e^2)}. \quad (20)$$

To analyze the dynamics of the spin vector, we go to co-rotating frame with $\hat{\mathbf{L}}$ about $\hat{\mathbf{L}}_{\text{out}}$, where Eq. (19) becomes

$$\left(\frac{d\mathbf{S}}{dt} \right)_{\text{rot}} = (\Omega_{\text{L}} \hat{\mathbf{L}}_{\text{out}} + \Omega_{\text{SL}} \hat{\mathbf{L}}) \times \mathbf{S}, \quad (21)$$

$$= \boldsymbol{\Omega}_{\text{e}} \times \mathbf{S}, \quad (22)$$

where we define

$$\boldsymbol{\Omega}_{\text{e}} \equiv \Omega_{\text{L}} \hat{\mathbf{L}}_{\text{out}} + \Omega_{\text{SL}} \hat{\mathbf{L}}, \quad (23)$$

$$\Omega_{\text{L}} \equiv -\frac{d\phi}{dt}. \quad (24)$$

In general, Eq. (22) is difficult to analyze, since Ω_{L} , Ω_{SL} and I all vary significantly within each LK cycle and change secularly over timescale $\sim t_{\text{GW}}(e)$. However, at times when both $t_{\text{GW}}(e) \gg \Omega_{\text{GR}}^{-1}$ and $t_{\text{GW}}(e) \ll j(e_{\text{max}}) t_{\text{LK}}$ are satisfied, the system can be treated as nearly periodic within each LK cycle¹. We can then rewrite Eq. (22) in Fourier components

$$\left(\frac{d\mathbf{S}}{dt} \right)_{\text{rot}} = \left[\bar{\boldsymbol{\Omega}}_{\text{e}} + \sum_{N=1}^{\infty} \boldsymbol{\Omega}_{\text{eN}} \cos\left(\frac{2\pi N t}{P_{\text{LK}}}\right) \right] \times \mathbf{S}. \quad (25)$$

The bar denotes an average over an LK cycle, and we write $\bar{\boldsymbol{\Omega}}_{\text{e}} \equiv \boldsymbol{\Omega}_{\text{e0}}$ for convenience. We adopt convention where $t = 0$ is the maximum eccentricity phase of the LK cycle. The Fourier components $\boldsymbol{\Omega}_{\text{eN}}$ then vary over timescales $\sim t_{\text{GW}}(e)$.

3.1. Component Form

For later analysis, it is also useful to write Eq. (25) in components. To do so, it is useful to define inclination angle \bar{I}_{e} as the angle between $\bar{\boldsymbol{\Omega}}_{\text{e}}$ and \mathbf{L}_{out} as shown in Fig. 3. To express \bar{I}_{e} algebraically, we first define LK-averaged quantities

$$\overline{\Omega_{\text{SL}} \sin I} \equiv \bar{\Omega}_{\text{SL}} \sin \bar{I}, \quad (26)$$

$$\overline{\Omega_{\text{SL}} \cos I} \equiv \bar{\Omega}_{\text{SL}} \cos \bar{I}. \quad (27)$$

¹ Note that apsidal precession is a non-dissipative effect, so the LK cycle is nearly periodic even when $\Omega_{\text{GR}} \gtrsim (j(e)t_{\text{LK}})^{-1}$.

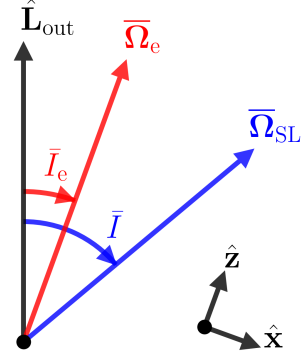


Figure 3. Definition of angles, shown in plane of the two angular momenta \mathbf{L}_{out} and \mathbf{L} . Note that for $I_0 > 90^\circ$, implying $\bar{I} > 90^\circ$, we have $\bar{I}_{\text{e}} < 0$ since $\Omega_{\text{L}} < 0$. The bottom right shows our choice of coordinate axes.

It then follows that

$$\tan \bar{I}_{\text{e}} = \frac{\mathcal{A} \sin \bar{I}}{1 + \mathcal{A} \cos \bar{I}}, \quad (28)$$

where

$$\mathcal{A} \equiv \frac{\bar{\Omega}_{\text{SL}}}{\Omega_{\text{L}}}. \quad (29)$$

To do so, we choose non-inertial coordinate system where $\hat{\mathbf{z}} \propto \bar{\boldsymbol{\Omega}}_{\text{e}}$ and $\hat{\mathbf{x}}$ lies in the plane of \mathbf{L}_{out} and \mathbf{L} with positive component along \mathbf{L} (see Fig. 3). In this reference frame, the polar coordinate is just θ_{e} as defined above in Eq. (34), and the equation of motion becomes

$$\frac{d\mathbf{S}}{dt} = \left[\bar{\Omega}_{\text{e}} \hat{\mathbf{z}} + \sum_{N=1}^{\infty} \boldsymbol{\Omega}_{\text{eN}} \cos\left(\frac{2\pi N t}{P_{\text{LK}}}\right) \right] \times \mathbf{S} - \bar{I}_{\text{e}} \hat{\mathbf{y}} \times \mathbf{S}. \quad (30)$$

One further simplification lets us cast this vector equation of motion into scalar form. Break \mathbf{S} into components $\mathbf{S} = S_x \hat{\mathbf{x}} + S_y \hat{\mathbf{y}} + \cos \theta_{\text{e}} \hat{\mathbf{z}}$ and define complex variable

$$S_{\perp} \equiv S_x + i S_y. \quad (31)$$

Then, we can rewrite Eq. 30 as

$$\begin{aligned} \frac{dS_{\perp}}{dt} = & i \bar{\Omega}_{\text{e}} S_{\perp} - \bar{I}_{\text{e}} \cos \theta_{\text{e}} + \sum_{N=1}^{\infty} [\cos(\Delta I_{\text{eN}}) S_{\perp} \\ & - i \cos \theta \sin(\Delta I_{\text{eN}})] \Omega_{\text{eN}} \cos N \Omega t. \end{aligned} \quad (32)$$

Here, for each $\boldsymbol{\Omega}_{\text{eN}}$ Fourier harmonic, we denote its magnitude Ω_{eN} and its inclination angle relative to \mathbf{L}_{out} as I_{eN} using the same convention as Fig. 3 (where $\bar{I}_{\text{e}} \equiv I_{\text{e0}}$), and $\Delta I_{\text{eN}} = \bar{I}_{\text{e}} - I_{\text{eN}}$.

4. ANALYSIS: DEVIATION FROM ADIABATICITY

In general, Eq. (25) is difficult to study analytically. Two possible simplifying approximations can be made: (i) the

effect of the $N \geq 1$ harmonic terms is negligible, or (ii) the Ω_{eN} Fourier coefficients all evolve very slowly compared to other dynamical timescales (i.e. $\dot{I}_{eN} \approx 0$). In this section, we analyze the former approximation and provide accurate analytic descriptions of dynamics. The latter approximation is studied in Section 5.

4.1. The Adiabatic Invariant

When neglecting the $N \geq 1$ harmonic terms, the equation of motion is modified to

$$\left(\frac{d\bar{\mathbf{S}}}{dt} \right)_{\text{rot}} = \bar{\Omega}_e \times \bar{\mathbf{S}}. \quad (33)$$

It is not obvious in what capacity analysis of Eq. (33) is applicable to Eq. (25). Empirically, we find that the LK-average of \mathbf{S} (which no longer has unit norm) often evolves following Eq. (33), which is why we have used the notation $\bar{\mathbf{S}}$. This is expected, as over timescales $\lesssim P_{\text{LK}}$ the evolution of \mathbf{S} should be dominated by the $N \geq 1$ harmonics we have neglected. An intuitive interpretation of this result is that the $N \geq 1$ harmonics vanish when taking the LK-average of Eq. (25).

Eq. (33) has one desirable property: θ_e , given by

$$\cos \theta_e \equiv \bar{\mathbf{S}} \cdot \hat{\bar{\Omega}}_e, \quad (34)$$

is an adiabatic invariant. The adiabaticity condition requires the precession axis evolve slowly compared to the precession frequency at all times:

$$\frac{d\bar{I}_e}{dt} \ll \bar{\Omega}_e. \quad (35)$$

Here, \bar{I}_e changes on timescale $t_{\text{GW}}(e)$ while

$$\bar{\Omega}_e \sim \max(\Omega_{\text{GR}}(e_{\text{max}}), j(e_{\text{max}})t_{\text{LK}}) j(e_{\text{max}}). \quad (36)$$

We see that the adiabatic assumption is more stringent than the condition for the Fourier decomposition in Eq. (25) to be valid by a factor $\sim j(e_{\text{max}})$.

4.2. Calculating Deviation from Adiabaticity

In real systems, the particular extent to which θ_e is conserved depends on how well Eq. (35) is satisfied. In this subsection, we derive a loose bound on the total non-conservation of θ_e , then in the next subsection we show this bound can be estimated from initial conditions.

When neglecting harmonic terms, the scalar equation of motion Eq. (32) becomes

$$\frac{dS_{\perp}}{dt} = i\bar{\Omega}_e S_{\perp} - \dot{I}_e \cos \theta_e. \quad (37)$$

This can be solved in closed form using an integrating factor. Defining

$$\Phi(t) \equiv \int_{-\infty}^t \bar{\Omega}_e dt, \quad (38)$$

we obtain solution up until some final time t_f

$$e^{-i\Phi} S_{\perp} \Big|_{-\infty}^{t_f} = - \int_{-\infty}^{t_f} e^{-i\Phi(\tau)} \dot{I}_e \cos \theta d\tau. \quad (39)$$

It can be seen that, in the adiabatic limit [Eq. (35)], $|S_{\perp}| = \sin \theta_e$ is indeed conserved, as the phase of the integrand in the right hand side varies much faster than the magnitude.

Recalling $|S_{\perp}| = \sin \theta_e$ and analyzing Eq. (39), we see that $\sin \theta_e \approx \theta_e$ oscillates about its value at $t = -\infty$ with amplitude

$$|\Delta \theta_e| \sim \frac{\dot{I}_e}{\bar{\Omega}_e}. \quad (40)$$

This is compared to the $\Delta \theta_e$ from simulations in the bottom center panels of Figs. 4 and 5 as the green line. We see that in the latter simulation, the faster merger, the order of magnitude of $|\Delta \theta_e|$ is somewhat well predicted, while in the slower merger a second contribution dominates $\Delta \theta_e$ oscillations, discussed in Section 5.

Furthermore, if we denote $|\Delta \theta_e|^f$ to be the total change in θ_e from $t = -\infty$ to merger, we can give loose bound²

$$|\Delta \theta_e|^f \lesssim \left| \frac{\dot{I}_e}{\bar{\Omega}_e} \right|_{\text{max}}. \quad (41)$$

4.3. Estimate of Deviation from Adiabaticity from Initial Conditions

To estimate $\left| \dot{I}_e / \bar{\Omega}_e \right|_{\text{max}}$ from initial conditions, we first differentiate Eq. (28),

$$\dot{I}_e = \left(\frac{\mathcal{A}}{\bar{\mathcal{A}}} \right) \frac{\mathcal{A} \sin \bar{I}}{1 + 2\mathcal{A} \cos \bar{I} + \mathcal{A}^2}. \quad (42)$$

It also follows from Eq. (23) that

$$\bar{\Omega}_e = \bar{\Omega}_L \left(1 + 2\mathcal{A} \cos \bar{I} + \mathcal{A}^2 \right)^{1/2}, \quad (43)$$

from which we obtain

$$\left| \frac{\dot{I}_e}{\bar{\Omega}_e} \right| = \left| \frac{\mathcal{A}}{\bar{\mathcal{A}}} \right| \frac{1}{\left| \bar{\Omega}_L \right|} \frac{\mathcal{A} \sin \bar{I}}{(1 + 2\mathcal{A} \cos \bar{I} + \mathcal{A}^2)^{3/2}}. \quad (44)$$

² Given the complicated evolution of $\bar{\Omega}_e$ and \dot{I}_e , it is difficult to give a more exact bound on the deviation from adiabaticity. In practice, deviations $\lesssim 1^\circ$ are observationally indistinguishable, so the exact scaling in this regime is negligible.

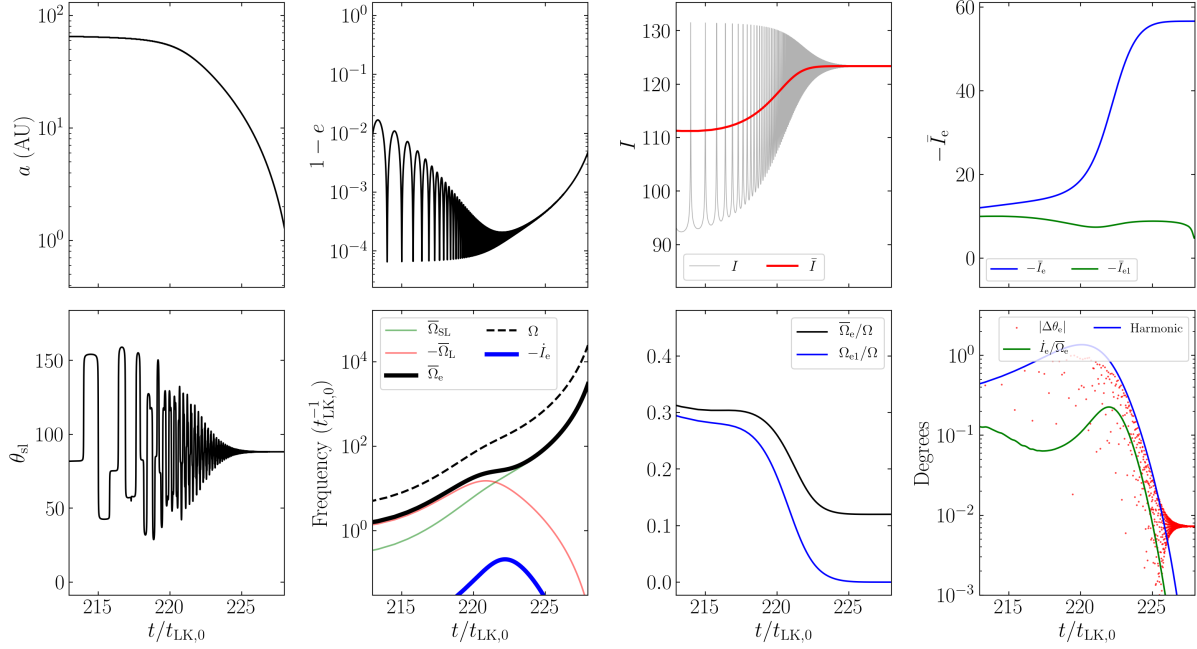


Figure 4. The same simulation as Fig. 1 but shown focusing on the region where $\mathcal{A} \approx 1$. The top three panels depict a , e , I and \bar{I} as before, but in addition I_e [Eq. (28)] and I_{e1} are shown in the third panel. The bottom three panels depict the frequency ratios between the zeroth and first Fourier components of Ω_e to the LK frequency $\Omega = 2\pi/P_{LK}$; the magnitude of oscillation of θ_e away from its initial value (red dots) as well as amplitude estimates due to non-adiabatic effects [green, Eq. (40)] and due to resonances with harmonic terms [blue, Eq. (59)]; and the same characteristic frequencies as before. In the bottom middle panel, it is clear that oscillations in θ_e are dominantly driven by interactions with the $N = 1$ harmonic.

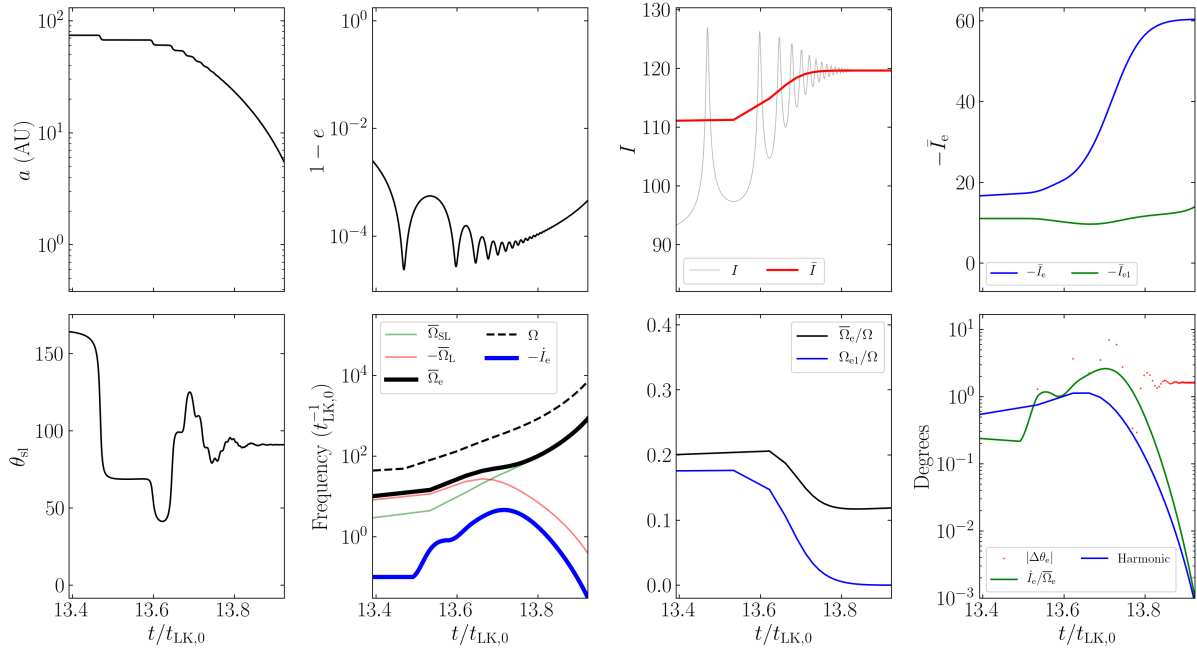


Figure 5. Same as Fig. 4 except for $I_0 = 90.2^\circ$, corresponding to a faster merger and a total change in θ_e of $\approx 2^\circ$. In the bottom middle panel, the nonadiabatic contribution is more significant and causes much poorer conservation of θ_e .

This is maximized when $\mathcal{A} \simeq 1$, and so we obtain that the maximum deviation should be bounded by

$$\left| \frac{\dot{I}_e}{\bar{\Omega}_e} \right|_{\max} \simeq \left| \frac{\dot{\mathcal{A}}}{\mathcal{A}} \right| \frac{1}{\left| \frac{\bar{\Omega}_L}{\bar{\Omega}_L} \right|} \frac{\sin \bar{I}}{(2 + 2 \cos \bar{I})^{3/2}}. \quad (45)$$

To evaluate this, we make two assumptions: (i) \bar{I} is approximately constant, and (ii) $j(e)$ evaluated at $\mathcal{A} \simeq 1$ can be approximated as a constant multiple of the initial $j(e_{\max})$, so that

$$j_{\star} \equiv j(e_{\star}) = f \sqrt{\frac{5}{3}} \cos^2 I_0, \quad (46)$$

for some unknown factor $f > 1$; we use star subscripts to denote evaluation at $\mathcal{A} \simeq 1$. f turns out to be relatively insensitive to I_0 . This can be as systems with lower e_{\max} values taking more cycles to attain $\mathcal{A} \simeq 1$, resulting in all systems experiencing a similar amount of decay due to GW radiation.

For simplicity, let's first assume $\mathcal{A} \simeq 1$ is satisfied when the LK oscillations are mostly suppressed, and $e_{\star} \approx 1$ throughout the LK cycle (we will later see that the scalings are the same in the LK-oscillating regime). Then we can write

$$\mathcal{A} \simeq \frac{3Gn(m_2 + \mu/3)}{2c^2 a j^2} \left[\frac{3 \cos \bar{I} + 3e^2/2}{4t_{\text{LK}} j} \right]^{-1}, \quad (47)$$

$$\simeq \frac{G(m_2 + \mu/3)m_{12}\tilde{a}_3^3}{c^2 m_3 a^4 j \cos \bar{I}}, \quad (48)$$

$$\propto \frac{1}{a^4 j}, \quad (49)$$

$$\frac{\dot{\mathcal{A}}}{\mathcal{A}} = -4 \left(\frac{\dot{a}}{a} \right)_{\text{GW}} + \frac{e}{j^2} \left(\frac{de}{dt} \right)_{\text{GW}}. \quad (50)$$

Approximating $e_{\star} \approx 1$ in Eqs. (9) and (10) gives

$$\left[\frac{\dot{\mathcal{A}}}{\mathcal{A}} \right]_{\mathcal{A}=1} \simeq \frac{64G^3 \mu m_{12}^2}{5c^5 a_{\star}^4 j_{\star}^7} \times 15, \quad (51)$$

$$\bar{\Omega}_{L,\star} \approx \frac{3 \cos \bar{I}}{2t_{\text{LK}} j_{\star}}, \quad (52)$$

$$\left| \frac{\dot{I}_e}{\bar{\Omega}_e} \right|_{\max} \approx \frac{128G^3 \mu m_{12}^2}{c^5 a_{\star}^4 j_{\star}^6} \frac{t_{\text{LK}}}{\cos \bar{I}} \frac{\sin \bar{I}}{(2 + 2 \cos \bar{I})^{3/2}}. \quad (53)$$

With the ansatz for j_{\star} given by Eq. (46) and requiring Eq. (48) equal 1 for a given j_{\star} and a_{\star} gives us the final expression

$$\left| \frac{\dot{I}_e}{\bar{\Omega}_e} \right|_{\max} \approx \frac{128G^3 \mu m_{12}^3 \tilde{a}_3^3}{c^5 \sqrt{G} m_{12} m_3} \left(\frac{c^2 m_3 \cos \bar{I}}{G(m_2 + \mu/3)m_{12}\tilde{a}_3^3} \right)^{11/8} \times (j_{\star})^{-37/8} \frac{\tan \bar{I}}{(2 + 2 \cos \bar{I})^{3/2}}. \quad (54)$$

The agreement of Eq. (54) with numerical simulation is remarkable, as shown in Fig. 6.

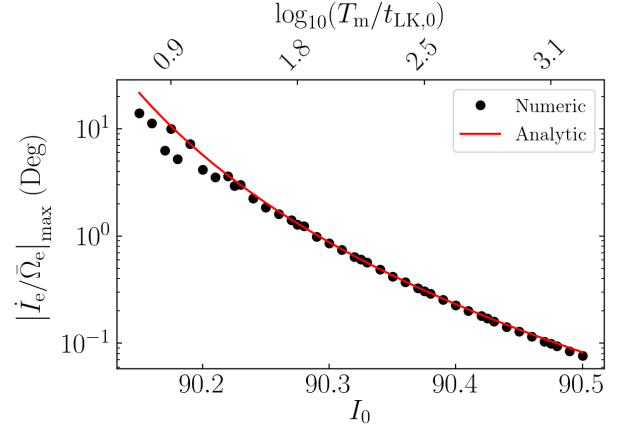


Figure 6. Comparison of $\left| \dot{I}_e / \bar{\Omega}_e \right|_{\max}$ extracted from simulations and using Eq. (54), where we take $f = 2.6$ in Eq. (46). The merger time P_m is shown along the top axis of the plot in units of the characteristic LK timescale at the start of inspiral $t_{\text{LK},0}$; the LK period is initially of order a few $t_{\text{LK},0}$. The agreement is remarkable for mergers that are more adiabatic (towards the right).

Above, we assumed that $\mathcal{A} \simeq 1$ is satisfied when the eccentricity is mostly constant (see Fig. 1 for an indication of how accurate this is for the parameter space explored in Fig. 6). It is also possible that $\mathcal{A} \simeq 1$ occurs when the eccentricity is still undergoing substantial oscillations. In fact, Eq. (54) is still accurate in this regime when replacing e with e_{\max} , due to the following analysis. Recall that when $e_{\min} \ll e_{\max}$, the binary spends a fraction $\sim j(e_{\max})$ of the LK cycle near $e \simeq e_{\max}$ (Anderson et al. 2016). This fraction of the LK cycle dominates both GW dissipation and $\bar{\Omega}_e$ precession. Thus, both terms in the expression $\dot{I}_e / \bar{\Omega}_e$ are evaluated near the maximum eccentricity and are suppressed by a factor of $j(e_{\max})$, which cancels out.

The accuracy of Eq. (54) in bounding the total change in $\Delta \theta_e^f$ over inspiral is shown in Fig. 7. Note that conservation of θ_e is generally much better than Eq. (54) predicts; cancellation of phases in Eq. (39) is generally more efficient than Eq. (54) assumes.

5. ANALYSIS: RESONANCES AND BREAKDOWN OF θ_E CONSERVATION

In the previous section, we neglected the $N \geq 1$ Fourier harmonics in Eq. (25). However, this assumption breaks down near certain resonances described below. For simplicity, we ignore the effects of GW dissipation in this section and assume the system is exactly periodic (and $\dot{I}_e = 0$). With these assumptions, the system resembles that studied in Storch & Lai (2015), but the dynamics turn out to be vastly different. Below, we present an analysis sufficient for the key results of this paper, and give a more formal treatment in Appendix A.

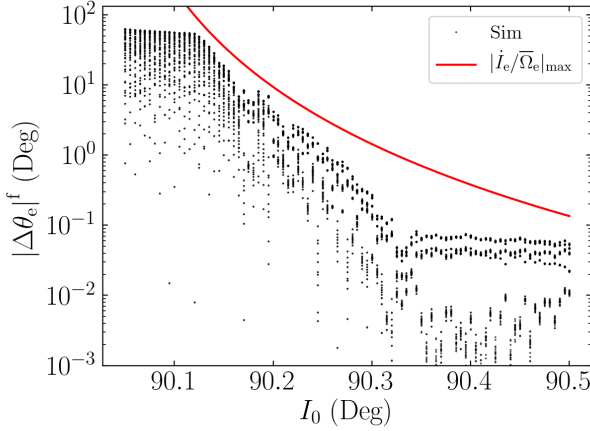


Figure 7. Total change in θ_e over inspiral as a function of initial inclination I_0 , where the initial $\bar{\Omega}_e$ is computed without GW dissipation. For each I_0 , 100 simulations are run for \mathbf{S} on a uniform, isotropic grid. Plotted for comparison is the bound $|\Delta\theta_e|^f \lesssim |I_e/\bar{\Omega}_e|_{\max}$, using the analytical scaling given by Eq. (54). It is clear that the given bound is not tight but provides an upper bound for non-conservation of θ_e due to nonadiabatic effects. At the right of the plot, the accuracy saturates: this is because neglecting GW dissipation causes inaccuracies when computing the average $\bar{\Omega}_e$.

When $I_e = 0$, the scalar equation of motion Eq. (32) is then:

$$\frac{dS_{\perp}}{dt} = i\bar{\Omega}_e S_{\perp} + \sum_{N=1}^{\infty} [\cos(\Delta I_{eN}) S_{\perp} - i \cos \theta \sin(\Delta I_{eN})] \Omega_{eN} \cos N\Omega t. \quad (55)$$

Resonances can occur when $\bar{\Omega}_e = N\Omega$. Since $\bar{\Omega}_e \lesssim \Omega$ for most regions of parameter space (see Fig. 9), we restrict our analysis to resonances with the $N = 1$ component. The two possible resonant behaviors are a parametric resonance [modulation of the oscillation frequency in Eq. (55)] and resonant forcing by the second term. Parametric resonances are typically very narrow and are therefore hard to excite as the system's frequencies change under GW dissipation. As such, we consider only the effect of the second term in Eq. (55).

Restricting our attention to $N = 1$ and neglecting the parametric term, the equation of motion reduces to

$$\frac{dS_{\perp}}{dt} \approx i\bar{\Omega}_e S_{\perp} - i \cos \theta_e \sin(\Delta I_{e1}) \Omega_{e1} \cos(N\Omega t). \quad (56)$$

We can approximate $\cos(N\Omega t) \approx e^{iN\Omega t}/2$, as the $e^{-iN\Omega t}$ component is far from resonance. Then we can write down

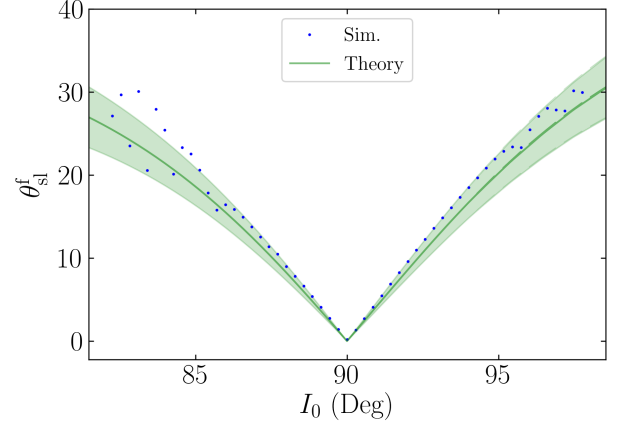


Figure 8. Plot of θ_{sl}^f for $m_1 = m_2 = m_3 = 30M_{\odot}$, $a_{in} = 0.1$ AU, $\bar{a}_3 = 3$ AU, $e_3 = 0$, where $e_0 = 0.001$ and $\theta_{sl}^i = 0$ over a restricted range of I_0 (analogous to the top panel of Fig. 4 in Liu & Lai 2017). The blue dots denote θ_{sl}^f obtained from numerical simulation. The green line gives θ_{sl}^f assuming perfect conservation of θ_e , and the green shaded area shows the expected deviation following Eq. (60).

solution

$$\Phi(t) = \int_0^t \bar{\Omega}_e d\tau, \quad (57)$$

$$e^{-i\Phi} S_{\perp} \Big|_{-\infty}^{\infty} = - \int_{-\infty}^{\infty} \frac{i \sin(\Delta I_{e1}) \Omega_{e1}}{2} e^{-i\Phi(\tau) + i\Omega\tau} \cos \theta_e d\tau. \quad (58)$$

Thus, similarly to Section 4.2, $|\Delta\theta_e|$ can be bound by

$$|\Delta\theta_e| \sim \frac{1}{2} \frac{\sin(\Delta I_{e1}) \Omega_{e1}}{|\Omega - \bar{\Omega}_e|}. \quad (59)$$

This is shown as the blue line in the bottom center panels of Fig. 4 and 5. We see that the amplitude of oscillations in θ_e are well described by Eq. (59), particularly in the former case (where the non-adiabatic contribution is weaker).

Again analogously to Section 4.2, we obtain loose bound for total nonconservation of θ_e

$$|\Delta\theta_e|^f \lesssim \frac{1}{2} \left| \frac{\sin(\Delta I_{e1}) \Omega_{e1}}{\Omega - \bar{\Omega}_e} \right|_{\max}. \quad (60)$$

If we assume the right hand side in Eq. (60) is maximized initially, we can predict $\Delta\theta_e^f$ for mildly LK-enhanced mergers (Liu & Lai 2017) rather well, as shown in Fig. 8.

While Eq. (59) depends on the properties of the $N = 1$ Fourier component, the conditions for substantial θ_e non-conservation can be understood in terms of physical quantities:

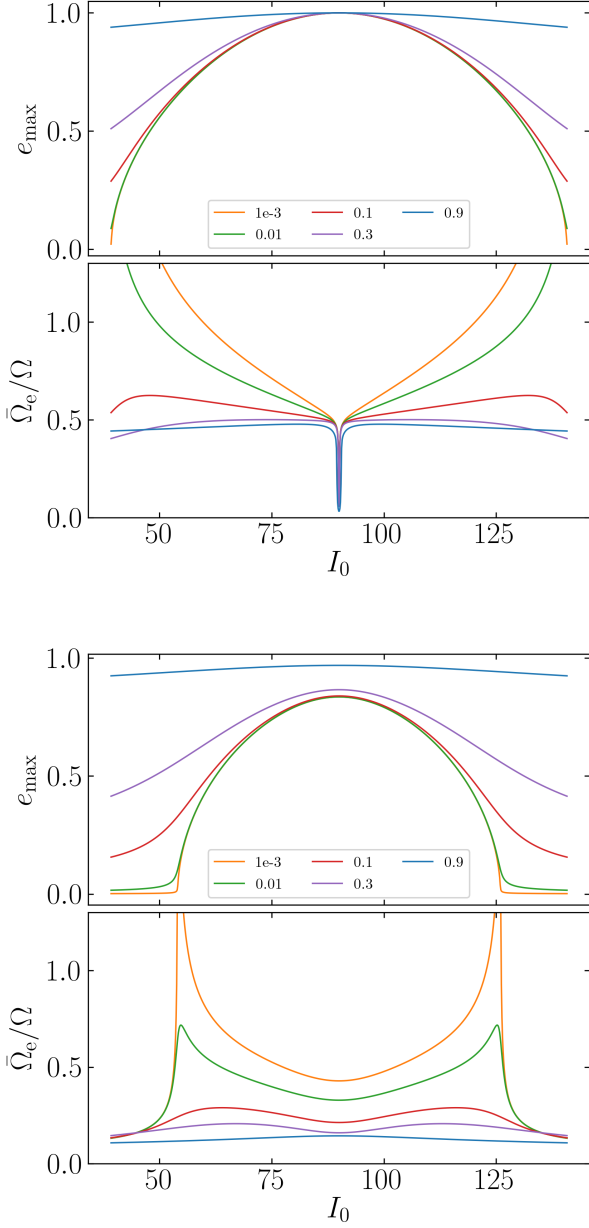


Figure 9. For the fiducial parameters (top two plots) and for the compact parameter regime studied in Fig. 8 and Liu & Lai (2017) (bottom two plots), e_{\max} and $\bar{\Omega}_e/\Omega$ as a function of I_0 for varying values of e_{\min} . Both smaller e_{\min} and e_{\max} values more easily satisfy the resonant condition $\bar{\Omega}_e/\Omega \approx 1$.

- $\sin(\Delta I_{e1})$ is small unless $\mathcal{A} \approx 1$. Otherwise, $\bar{\Omega}_e$ does not nutate appreciably within an LK cycle, and all the $\bar{\Omega}_{eN}$ are aligned with $\bar{\Omega}_e$, implying all the $\Delta I_{eN} \approx 0$.

- Smaller values of both e_{\min} and e_{\max} increase $\bar{\Omega}_e/\Omega$, as shown in Fig. 9, strengthening the interaction with the $N = 1$ resonance.

LK-driven coalescence causes \mathcal{A} to increase on a similar timescale to that of e_{\min} increase (see Fig. 1). As such, we conclude that the effect of harmonic terms generally only affects θ_e conservation when $\mathcal{A} \approx 1$ initially.

6. CONCLUSION AND DISCUSSION

Relation between θ_e and θ_{sl}^f , as a function of I .

The “chaotic” behavior in Paper I is because it satisfies the heuristic provided at the end of the harmonics section well.

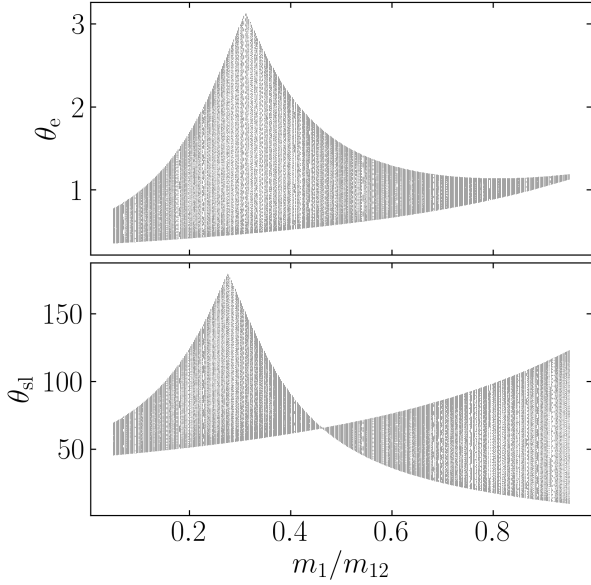
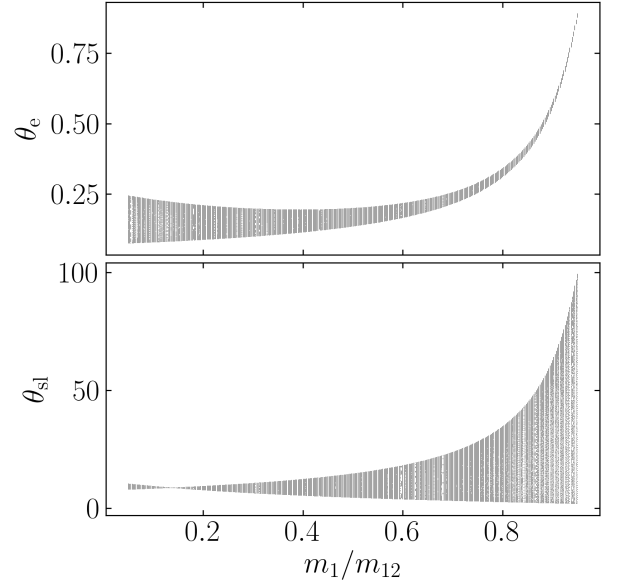
Interestingly, harmonic terms begin to dominate $\Delta\theta_e$ at quite small inclinations $I_0 \lesssim 90.35^\circ$, but the non-adiabatic contribution to nonconservation obviously dominates out to $I_0 \approx 90.4^\circ$.

REFERENCES

- Anderson, K. R., Storch, N. I., & Lai, D. 2016, Monthly Notices of the Royal Astronomical Society, 456, 3671
- Kozai, Y. 1962, The Astronomical Journal, 67, 591
- Lidov, M. L. 1962, Planetary and Space Science, 9, 719
- Liu, B., & Lai, D. 2017, The Astrophysical Journal Letters, 846, L11
- . 2018, The Astrophysical Journal, 863, 68
- Peters, P. C. 1964, Physical Review, 136, B1224

Storch, N. I., & Lai, D. 2015, Monthly Notices of the Royal
Astronomical Society, 448, 1821

APPENDIX

Figure 10. $I_0 = 70^\circ$ Figure 11. $I_0 = 88^\circ$

A. NONDISSIPATIVE SPIN DYNAMICS

A.1. Floquet Analysis

In this appendix, we consider the dynamics of the equation of motion

$$\frac{d\mathbf{S}}{dt} = \mathbf{\Omega}_e \times \mathbf{S}, \quad (\text{A1})$$

where $\mathbf{\Omega}_e$ is exactly periodic with period P_{LK} . This corresponds to taking the $t_{GW} \rightarrow \infty$ limit of the systems considered in the main text.

When analyzing a system bearing superficial resemblance to Eq. (A1), Storch & Lai (2015) (hereafter SL15) found chaotic dynamics due to resonance overlap. The hallmark of chaos in their study is the presence of fine structure in a bifurcation diagram (Fig. 1 of SL15) that shows the oscillation amplitude of a misalignment angle θ_{sl} when varying system parameters. To generate an analogous bifurcation diagram for our problem, we perform the following procedure: begin with $\mathbf{S} \parallel \mathbf{L}$, then evolve Eq. (A1) while sampling both θ_{sl} and θ_e at eccentricity maxima. We repeat this procedure while varying the mass ratio m_1/m_{12} of the inner binary, which only changes Ω_{SL} without changing the orbital evolution. θ_e turns out to be the best analog to the angle θ_{sl} in SL15. We show the results of this exercise in Figs. 10 and 11.

It can be observed that the bifurcation diagram is smooth and does not exhibit small scale structure, suggesting that Eq. (A1) does not produce chaotic behavior. We can understand this using Floquet theory, as Eq. (A1) is a linear

system with periodic coefficients (the system studied in SL15 is nonlinear, and so generates resonances that can overlap). Floquet's theorem says that when a linear system with periodic coefficients is integrated over a period, the evolution can be described by a linear transformation, the *monodromy matrix* \mathbf{M} (TODO this needs to be better worded).

In our problem, \mathbf{M} must be a proper orthogonal matrix, as it represents the effect of many infinitesimal rotations about $\mathbf{\Omega}_e$. Since \mathbf{M} is a 3×3 matrix, its eigenvalues must be 1 and two other roots of unity that are complex conjugates of one another. Denote the eigenvector with eigenvalue 1 by \mathbf{R} , then we have proven that Eq. (A1) consists of rotation about \mathbf{R} every P_{LK} . Chiefly, it cannot be chaotic.

Numerically, we find that $\mathbf{R} \approx \overline{\mathbf{\Omega}}_e$ except near the sorts of resonances described in Section 5.

Toy model?